

Defects in a Laser Powder Bed Fused Tool Steel

Jan Platl,* Harald Leitner, Christoph Turk, Ali Gökhan Demir, Barbara Previtali, and Ronald Schnitzer

Compared to conventional fabrication methods, additive manufacturing (AM) introduces new opportunities in terms of design freedom and part complexity due to the incremental layer-by-layer process. For tooling applications, higher cutting speeds can be realized by implementing of internal cooling channels in tools that could not be fabricated otherwise. However, processability of high-alloyed tool steels with laser powder bed fusion (LPBF) faces certain restrictions. In addition to pore formation, severe cracking caused by a combination of process-related stresses due to the high thermal gradient and susceptible materials may occur. This work aims to clarify the occurrence of process-related defects in dependence of the applied energy input of a high-alloyed cold-work tool steel and to correlate it to the evolution of microstructure respectively solidification structure. Defect surfaces and structural evolution are investigated. The results exhibit that with increasing energy input porosity changes from lack-of-fusion to keyhole porosity. Most recently published investigations suggest cold cracking as predominant failure mechanism during LPBF of tool steels. However, for the investigated material, the present study clearly reveals that, irrespective of the chosen energy input, hot cracks are formed. Crack propagation can be connected to the solidification structure and possible thermal stress accumulations caused by the process.

thicknesses in the order of tens of microns for powder-bed-based processes, the technique is restricted to small quantities of near-net-shaped parts.^[1,2]

For metals, the predominant AM techniques are the aforementioned powder-bed-based processes, such as electron beam melting (EBM) and laser powder bed fusion (LPBF) which is also known as selective laser melting (SLM^[3]). The main difference between these two processes is the source of energy input (electron beam and laser beam respectively). With EBM, typically processed materials are, for example, copper-based alloys due to the increased power absorptivity compared with the usually used Nd:YAG lasers^[4] or titanium-aluminides which require manufacturing temperatures of the surrounding powder bed above 1000 °C to avoid cracking during cooling.^[5] For the latter, EBM provides the opportunity to defocus the electron beam and therefore preheating of the entire powder bed layer in advance to the actual melting step is enabled. In comparison to LPBF, EBM

1. Introduction

Additive manufacturing (AM) enables the fabrication of parts made of metals, ceramics, composites, or polymers with highly complex geometries which cannot be manufactured in conventional subtractive processing routes, such as turning, milling, or drilling. However, due to the time-consuming manufacturing process caused by the layerwise production of parts with layer

facilitates much higher scan speeds. LPBF is more widely used for the fabrication of a larger variety of metals, such as nickel-based alloys and steels, as it provides advantages in terms of cost efficiency compared with EBM.^[6] The LPBF process features extraordinarily high cooling rates yielding extremely fine microstructures in comparison to conventional casting processes. Already built layers undergo a complex thermal cycle comprising of local remelting as well as in situ heat treatment, such as tempering. Due to the localized energy input through laser irradiation, a rather inhomogeneous microstructure with clearly visible heat-affected zones evolves.^[1]

The energy input is often illustrated by means of the so-called volumetric energy density (VED) which can be calculated using Equation (1) by inserting the laser powder P , the scan velocity v , the hatch distance h , and the layer thickness D .^[7]

$$VED = P / (v \cdot h \cdot D) \quad (1)$$


The resulting VED is commonly given in J mm^{-3} .

In recent years, the demand for manufacturing tools with LPBF increased as the incremental layer-by-layer build-up process provides the opportunity to realize either internal cooling channels or to directly produce near-net-shaped tools. This promises increased productivity through enhanced cutting velocities for drills or milling cutters made of high-speed steel,^[8] better

J. Platl, Prof. R. Schnitzer
Department of Materials Science
Montanuniversität Leoben
Franz-Josef-Straße 18, Leoben 8700, Austria
E-mail: jan.platl@unileoben.ac.at

Dr. H. Leitner, Dr. C. Turk
High Performance Metals Division
voestalpine Böhler Edelstahl GmbH & Co KG
Mariazellerstraße 25, Kapfenberg 8605, Austria

Dr. A. G. Demir, Prof. B. Previtali
Department of Mechanical Engineering
Politecnico di Milano
Via La Masa 1, Milan 20156, Italy

 The ORCID identification number(s) for the author(s) of this article can be found under <https://doi.org/10.1002/adem.202000833>.

DOI: 10.1002/adem.202000833

thermal control and thus shorter cycle-times using injection-molding inserts made of hot-work tool steel^[9] or reduced post-processing of tools for cold-work applications, such as stamping, punching, or cutting dies. As maraging steel grades (e.g., X3NiCoMoTi18-9-5) show good processability with LPBF due to the absence of hard carbon martensite, a lot of effort for the determination of optimized process parameters, the characterization of the microstructure, the mechanical properties, the fatigue behavior, and the post-process heat treatments has been made in the last years.^[10]

In comparison to maraging steels, less research effort has been carried out in the field of carbon-containing tool steels due to their less promising processability with LPBF. A general investigation on the formation of residual stresses in a low-alloyed tool steel with a carbon content of 0.45 wt% was performed by Chen et al.^[11] They conducted finite-element analysis to simulate the temperature profiles within one single melt pool in dependence of the applied VED and concluded that differently fine regions evolve after solidification of this single melt pool due to varying temperature gradients. This results in the formation of residual stresses because of inhomogeneous deformation caused by thermal stresses. In addition to these process-related stresses, residual stresses arise due to phase transformations during rapid cooling. The high-carbon content of conventional tool steels (hot-work, cold-work, and high-speed steels) guarantees a transformation from austenite to carbon martensite. The latter is susceptible to cracking due to its low ductility. To reduce the process-related thermal gradient and to suppress martensitic transformations and therefore to avoid cracking, the building platform can be preheated up to temperatures above martensite start temperature.^[12] In several recently published articles, the influence of building platform preheating was investigated. Mertens et al.^[13] analyzed the impact of different preheating temperatures on the evolution of residual stresses in the top layers of H13 (X40CrMoV5-1) hot-work tool steel processed with LPBF. They reported a change from compressive stresses at preheating temperatures up to 200 °C caused by the volume expansion during martensite formation to tensile stresses at 300 and 400 °C due to suppression of the martensite formation by exceeding the martensite start temperature. Krell et al.^[14] reported a decrease in crack density caused by a reduced temperature gradient as well as lower elastic moduli at elevated temperatures and therefore a reduction in residual stresses in the processed hot-work tool steel due to preheating of the building platform. Boes et al.^[15] also concluded that crack density of a selectively laser molten X65MoCrWV3-2 steel can be reduced by applying preheating temperatures up to 300 °C. The same conclusions were drawn by Geenen et al.,^[16] who observed a strong decrease in crack density by applying a platform temperature of 300 °C during LPBF of a high-alloyed M3:2 high-speed steel (HS 6-5-3 with 1.20 wt% carbon). Microscopically crack-free production of high carbon-containing tools was reported in the publications of Saewe et al.^[17] (processed powder: 80MoCrV42-16) and Feuerhahn et al.^[18] (processed powder: X110CrMoVA18-2) by applying platform temperatures of 200 and 240 °C, respectively. The platform preheating methods in LPBF are limited to external heat sources, such as resistive heaters placed beneath the base plate. Conventional LPBF systems are characterized by preheating temperatures below 400 °C. Higher temperatures exceeding

800 °C are achievable via novel machine architectures; however, the machine thermal stability becomes an important issue.^[19] Another promising approach to manufacture crack-free tool steel samples with high relative densities is provided by EBM. Jin et al.^[20] used this method to decrease the process-related temperature gradient and thus to produce crack-free high-speed steel samples with a carbon content of 1.64 wt% applying a preheating of the entire powder bed layer of ≈ 800 °C by defocusing the electron beam in advance to each melting step.

In addition to crack formation caused by phase transformations and thermal stresses, also hot cracking is a well-known phenomenon during conventional welding processes of high-alloyed steel grades. The formation of hot cracks has been investigated mainly during welding of stainless steels.^[21] These cracks evolve due to a combination of low-melting phases, which are mainly formed by sulfur and phosphorus, and stresses caused by the volume reduction during solidification and by shrinkage during cooling. As delta ferrite exhibits a higher solubility for these impurities compared with austenite, hot cracking susceptibility can be significantly reduced by guaranteeing at least a partly ferritic solidification path.^[22] The characteristic feature for the identification of a hot crack are freely solidified dendrites on the crack surface.^[23] Cloots et al.^[24] investigated crack surfaces of LPBF manufactured samples and found such freely solidified dendritic structures in a nickel-based alloy. They analyzed grain boundary segregations using atom probe tomography (APT) in combination with thermodynamic calculations and concluded a strong decrease in the melting point of the investigated IN738LC alloy due to enrichment of the element zirconium.

In addition to cracking, pore formation is another commonly known effect that may occur during LPBF. Geenen et al.^[16] revealed that very low energy input manifests itself in high porosity. The formed lack-of-fusion pores are irregularly shaped. Another type of porosity are the so-called keyhole pores which are spherically shaped. These pores are caused by excessively high laser energy input leading to inclusion of evaporated metal by the surrounding melt during solidification.^[25] In addition, this excessively high energy input was reported to yield increased crack densities due to intensified residual stresses.^[15,16] A less explored method for conveying higher energy input is through the use of multiple passes. It has been shown that multiple passes can be useful for reducing the porosity and residual stresses without the excessive energy input at a single layer.^[26]

However, there is a lack of detailed studies on crack characterization and identification of the prevailing cracking mechanism in high-alloyed tool steels manufactured by LPBF. Therefore, the aim of the present study is the clarification of this prevailing failure phenomenon and the general characterization of defects formed during LPBF of a high-alloyed cold-work tool steel. To simplify this manufacturing process and to confine the effective energy input to laser irradiation, LPBF experiments were carried out without preheating the building platform. A wide VED range was used to fabricate samples that were subsequently investigated to shed light on the influence of different energy inputs on the evolution of the defect structure. So-called step specimens, in which a varying number of welding bead layers are built, were manufactured to analyze the influence of different sample heights with respect to defect formation due to a varying thermal history during LPBF. Special interest was

drawn to crack surface characterization to clarify whether cold or hot cracking is present in the investigated material. Furthermore, possible correlations between defect formation and structural evolution were evaluated by means of light optical microscopy (LOM) and scanning electron microscopy (SEM). The obtained results are discussed and promising theories regarding elimination of cracks during LPBF of cold-work tool steels are proposed.

2. Experimental Section

2.1. Powder Characterization

For the LPBF process, argon gas atomized cold-work tool steel powder with a particle size fraction of 15–45 μm was used. The powder was produced and subsequently sieved to separate the desired fraction by voestalpine Böhler Edelstahl GmbH & Co KG, Kapfenberg, Austria. In **Table 1**, the chemical composition of the investigated powder, which was determined using inductively coupled plasma optical emission spectroscopy, is shown. The particle size distribution (PSD) of the powder was determined using a CAMSIZER XT from Retsch Technology GmbH. In addition to the PSD and the cumulative area fraction, which are shown in **Figure 1a**, the average particle diameters (D10, D50, and D90) were extracted from this measurement which is based on digital image analysis. The apparent density was determined in accordance with ASTM B212^[27] using a 2.5 mm Hall flowmeter funnel and resulted in a value of 4.10 g cm^{-3} . Particle morphology of loose powder was investigated with a ZEISS EVO 50 SEM in secondary electron (SE) detection mode at a working distance of 10 mm, see **Figure 1b**. The powder exhibits spherical particles with few satellites. To display possible internal pores and the solidification structure of powder particles after the atomization process, a cross-sectional micrograph was analyzed in backscattered electron (BSE) mode. To ensure better contrast, the sample underwent a mechanical polishing step with STRUERS oxide polishing suspension

Table 1. Chemical composition of the investigated gas atomized powder.

[wt%]	C	Si	Mn	Ni	P	S	Cr	W	Mo	V	Co
Powder	0.85	0.53	0.36	0.19	0.019	0.011	4.25	2.46	2.72	2.01	4.35

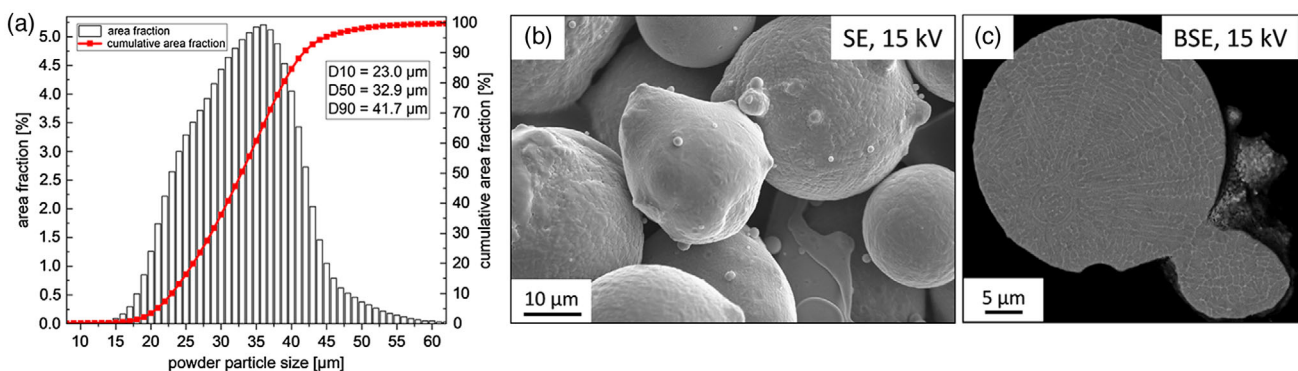


Figure 1. a) PSD and cumulative area fraction of the investigated powder and SEM micrographs of b) spherical, gas atomized powder particles with adjacent satellites and c) the dendritic solidification structure of a representative powder particle without internal porosity.

(OPS, 20 N for 1 min) after grinding and mechanical polishing down to 1 μm . **Figure 1c** exhibits an exemplary cross-section of a spherical, embedded powder particle with an adjacent satellite. In addition to this, for the gas atomization process typical powder morphology and the dendritic solidification structure, no internal porosity was found.

2.2. LPBF Processing

All samples were fabricated by a Renishaw AM250 machine with a reduced building volume system. As protective gas, argon with a maximum oxygen content of 0.1% was used. The machine operates with a fiber laser in pulsed emission regime by power modulation and for sample processing its maximum power P of 200 W and a focal diameter at the powder bed height of 70 μm was used. The layer thickness D was held constant at 30 μm . A process parameter study with the objective to determine suitable parameters for so-called step experiment samples with moderate porosity was conducted. For this purpose, cubic samples ($10 \times 10 \times 10 \text{ mm}^3$) were manufactured on an unalloyed building platform material ($\approx \text{C15 steel}$). The VED was varied between 35 and 252 J mm^{-3} to investigate the influence of various energy inputs on the evolution of defects and microstructure. Different VEDs were adjusted by varying the pulse duration t and the point distance d_p . In addition, minor variations of the hatch distance h were performed. Equation (2) can be used to calculate VED specifically for a LPBF using pulsed wave emission.

$$\text{VED} = P \cdot t / (d_p \cdot h \cdot D) \quad (2)$$

The specimens were produced without any upskin or downskin strategies. The border parameters were matched with the volume melting parameters except for the hatch distance. For the step experiments, in which different numbers of layers ($N = 1, 2, 3, 10, 50, 100, 500$, and 1000) were manufactured, a parameter with a VED of 67 J mm^{-3} was chosen. These samples with a base area of $10 \times 10 \text{ mm}^2$ and the corresponding height were built on conventionally manufactured cold-work tool steel material with almost the same composition as the powder (**Table 1**). An overview of the fabricated samples on the building platform is shown in **Figure 2**. All investigated samples in this work were manufactured without preheating of the building platform.

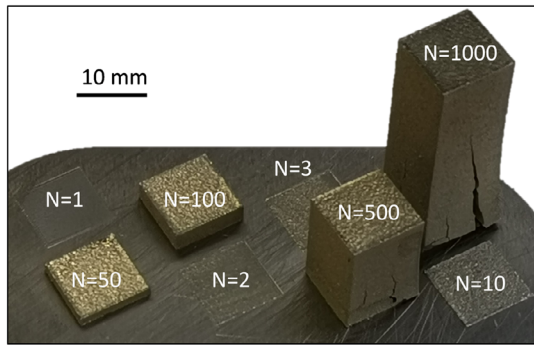


Figure 2. Macroscopic view of the building platform with the investigated step specimens. No visual delamination or cracking can be observed for the lower specimens up to 100 layers. For the higher specimens, severe cracking, especially in the lower regions adjacent to the building platform, is visible.

Due to the combination of mostly spherical powder particles, a moderate number of satellites attached to these particles and the narrow PSD, good processability in terms of powder spreading can be guaranteed. This is in accordance with desired properties for sufficient powder flowability proposed by Kumar.^[28] Samples with one, two, or three layers showed mostly remelting of the building platform because a high percentage of the laser energy is introduced into the building platform. This can be attributed first to a local lack of material due to unsteady powder spreading in early process stages and second to the low relative powder density of $\approx 52\%$ (compared to the theoretical density of pure iron of 7.874 g cm^{-3}).^[29] Therefore, process stability in terms of reproducible powder spreading and thus build-up of parts or samples can be assured only after spreading and melting a minimum of ten layers.

2.3. Defect and Microstructure Characterization

For defect structure evaluation in dependence of the applied VED, cross-sectional samples of the parameter study as well as step experiment specimens were characterized in polished condition without chemical etching. Metallographic preparation of the exemplary cross-section polishes ($N = 50, 1000$) included mechanical grinding and polishing down to $1 \mu\text{m}$ with subsequent vibro-polishing with OPS. For structural characterization, the samples were contrasted with diluted WII etchant for the LOM analysis and with 3% Nital etchant for the SEM investigations. Macroscopic crack analysis of the samples was carried out using a ZEISS Discovery.V20 stereo microscope. More detailed crack, porosity, and microstructure analysis (samples $N = 50, 1000$) were performed with a ZEISS Axio Imager M1m LOM and a TESCAN CLARA SEM in SE mode with acceleration voltages of $10\text{--}15 \text{ kV}$ at a working distance of 10 mm .

X-ray diffraction (XRD) phase analysis was conducted using a BRUKER D8 Advance with $\text{Cu K}\alpha$ radiation, a Bragg angle range of $30^\circ < 2\theta < 100^\circ$ and an increment of 0.02° . The dwell time was set to 1.2 s per step and the sample rotated with 50 rpm to achieve one full rotation per dwell time. Phase analysis was performed using Rietveld refinement with TOPAS software by

BRUKER. As carbide phase fractions of the investigated samples were too low to be quantified accurately, only austenite and martensite structure files were used for the refinement. The measurement of the top layers was conducted on the initial surface of the specimen after the LPBF process (as-built condition). The measurement of tempered layers was conducted on a grinded and subsequently polished cross-sectional sample ($N = 500$).

Constant strain-rate nanoindentation tests were performed on an InSEM nanoindenter (Nanomechanics, Inc.). The maximum penetration depth of the used Berkovich diamond tip was set to 250 nm and a grid of $105 \times 150 \mu\text{m}^2$ with a spacing of $5 \mu\text{m}$ between adjacent indents was tested. Hardness values were averaged from the measured data in the indentation depth range between 200 and 240 nm . The investigated sample ($N = 500$) was grinded and mechanically polished down to $1 \mu\text{m}$ and subsequently vibro-polished with OPS for 5 h to guarantee a completely scratch-free sample.

3. Results

3.1. Defect Characterization

To evaluate the influence of the VED on defect formation during LPBF, samples that were manufactured in a broad range of energy inputs were analyzed in the as-built state. Representative samples for low (40 J mm^{-3}) and high VED (204 J mm^{-3}), respectively, were characterized. In addition, a medium VED of 67 J mm^{-3} resulting in moderate porosity ($< 1\%$) was chosen to assess the influence of varying sample heights by means of step experiments. Figure 2 shows the building platform with these step specimens, in which a different number of layers N were manufactured. A visual examination is suggestive of having delamination- and crack-free parts up to a height of 100 layers ($\approx 3 \text{ mm}$). However, the cross-sectional LOM micrograph of the specimen with 50 layers, which is shown in Figure 3a, already reveals the presence of cracks in this sample at the corners in the transition zone to the building platform. With increasing sample height, additional cracks appear originating from the edges of the samples. Because of these significant differences in the macroscopic crack appearance of samples with varying heights, an exemplary 3D illustration of crack evolution is demonstrated by the highest sample ($N = 1000$) in Figure 3b. From the cross-sectional LOM image in Figure 3c, it can be seen that, as mentioned earlier, crack initiation originates from the edges of the samples and from the transition zones between additively manufactured material and building platform. In addition, Figure 3b,c show that in addition to the almost symmetrically arranged crack origin heights on both sides of the cross-section, all of the cracks propagate toward the top of the specimens. To clearly evaluate the predominant cracking mechanism, crack surfaces were analyzed by means of SEM. The black and white arrows in Figure 3 indicate positions of cracks which were analyzed. The crack surfaces of the 1000 layer step specimen as well as those of the aforementioned representative specimens for low and high VED were exposed by cooling the samples in liquid nitrogen and subsequently opening the cracks by usage of a chisel and a hammer. Due to cooling of the sample,

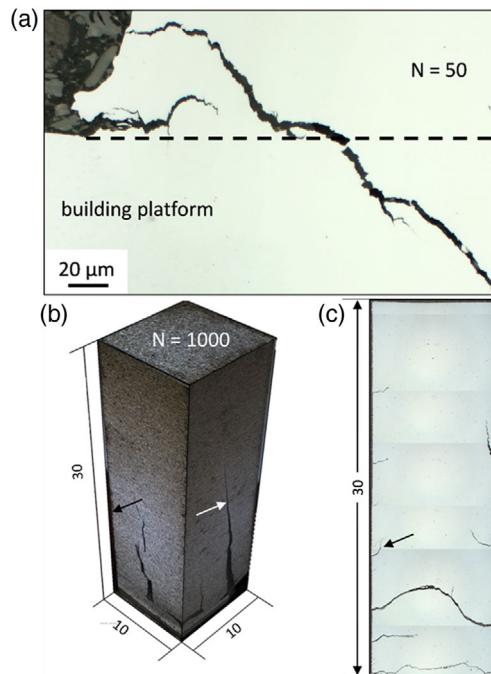


Figure 3. a) Unetched cross-section of the sample with 50 layers; the black dashed line indicates the transition zone between building platform and AM material. Illustration of the specimen with 1000 layers: b) 3D overview and c) cross-sectional LOM image. The dimensions are given in mm and the black and white arrows indicate crack positions which were subsequently examined using SEM.

a brittle forced fracture is guaranteed which can be distinguished from the already existing crack surface.

In addition to crack surfaces, exemplary porosity formation in dependence of the applied VED was investigated by means of

LOM and SEM images in which the building direction of the LPBF process is indicated by the white arrows in the upper left corners of the images. In **Figure 4a**, irregularly formed pores can be seen in the LOM image of the sample with very low energy input of 40 J mm^{-3} . Furthermore, an unmelted powder particle in such a pore is visible (indicated by the black arrow in **Figure 4a**). The same type of porosity is shown in the SEM image of the sample with 50 layers manufactured with a medium VED of 67 J mm^{-3} , see **Figure 4c**. In addition to the micro cracks initiating from the edge of the strongly oxidized inner pore surface, needle-like microstructural constituents and brightly depicted dendritic structures can be observed. In addition to the weld bead layer structure and the crack originating from the sample edge in **Figure 4d**, an almost spherically shaped pore with a crack can be seen in the same sample. It seems that the crack from the sample edge does not grow straight into the sample but propagates rather in a kind of zig-zag movement. The LOM image of the sample manufactured with a VED of 204 J mm^{-3} in **Figure 4b** also shows a spherically shaped pore similar to that shown in **Figure 4d**. Similar to **Figure 4d**, a crack initiating from the pore edge grows upward. In **Figure 4e**, a detailed view of the crack in **Figure 4d** is shown. Here, it is clear that this crack propagates along the dendritic structures which can be seen within the pore. It appears as if the crack propagation branches out according to the orientations of primary dendrite packages, which are indicated by the dashed black arrows.

In **Figure 5a**, an overview of the crack surface of the specimen with 1000 layers ($\text{VED} = 67 \text{ J mm}^{-3}$) is shown. The crack surface exhibits indications of dendritic structures. In addition, a fine zig-zag crack network propagating along the boundaries of these dendritic structures can be seen. **Figure 5b** provides a detailed insight on this crack surface and clearly reveals freely solidified dendrites. These images were taken at the position indicated by the black arrow in **Figure 3**. The second examined position (white

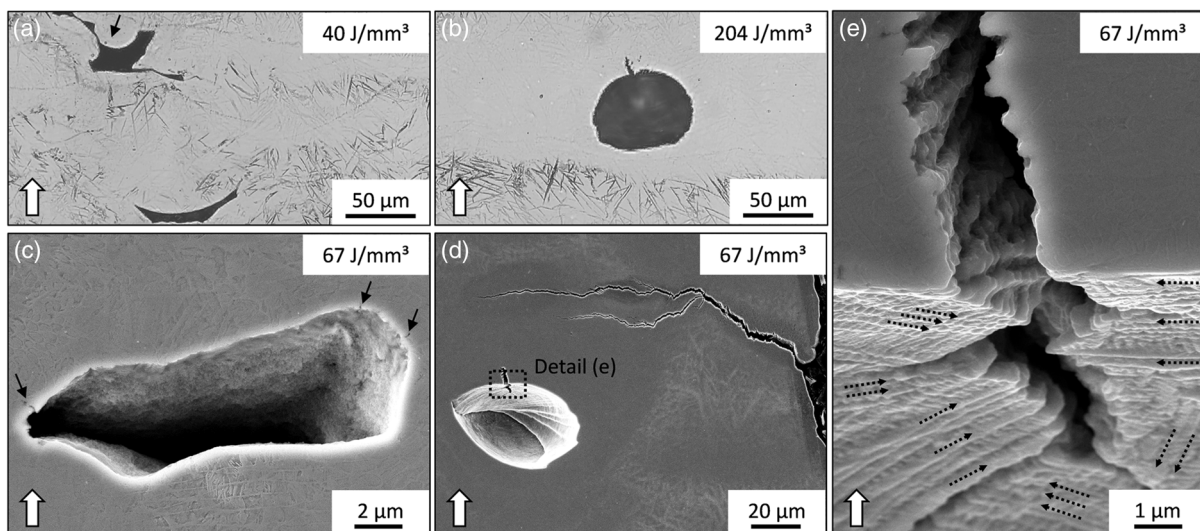


Figure 4. LOM and SEM images of a,c) irregularly formed pores and b,d) spherically shaped pores in different samples with varying VED. e) Magnified view of the crack and the dendritic structure inside the keyhole pore. The orientations of dendrite packages are indicated by the dashed black arrows. The black arrow in (a) indicates an unmelted powder particle and those in (c) indicate micro cracks starting from the edge of the strongly oxidized pore. The white arrows indicate the building direction.

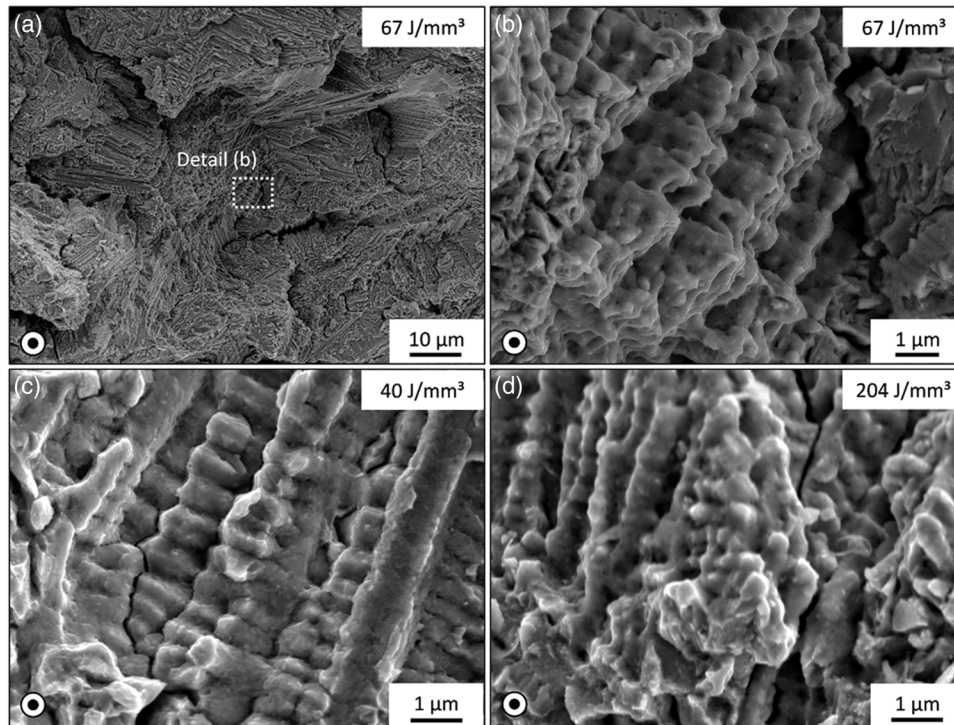


Figure 5. SEM images of crack surfaces at different magnifications in samples manufactured with varying VED. Irrespective of the applied energy input, all images exhibit a crack network and freely solidified dendrites. The white symbols indicate the building direction.

arrow in Figure 3b) gives the same impression. Crack surfaces of samples built with lower (40 J mm^{-3}) and higher VED (204 J mm^{-3}) are shown in Figure 5c,d, respectively. In both SEM images, similar dendritic surfaces can be seen and therefore the crack surfaces provide the same impression as for the sample manufactured with an energy input of 67 J mm^{-3} . In addition, Figure 5c again indicates crack propagation along dendrite boundaries.

3.2. Microstructural Characterization

Representative microstructural characterization has been carried out on an as-built sample manufactured with a VED of

67 J mm^{-3} ($N = 50$). **Figure 6a** shows that the top layers exhibit a different microstructure than the layers below. The latter are tempered multiple times during manufacturing of overlying layers compared with the surface layers. These tempered layers reveal dark needle-like structures and bright phases in the LOM. The inset in Figure 6a shows a magnified view of the top layers, which were not tempered during the process. Herein, no dark needle-like structures can be found. The images reveals a dendritic structure within the single weld bead layers which is oriented inversely to the thermal gradient. This orientation direction is indicated by the black arrows. In addition, a spherical shaped pore can be seen and again two cracks originate from the pore edge, which propagate along the direction marked by

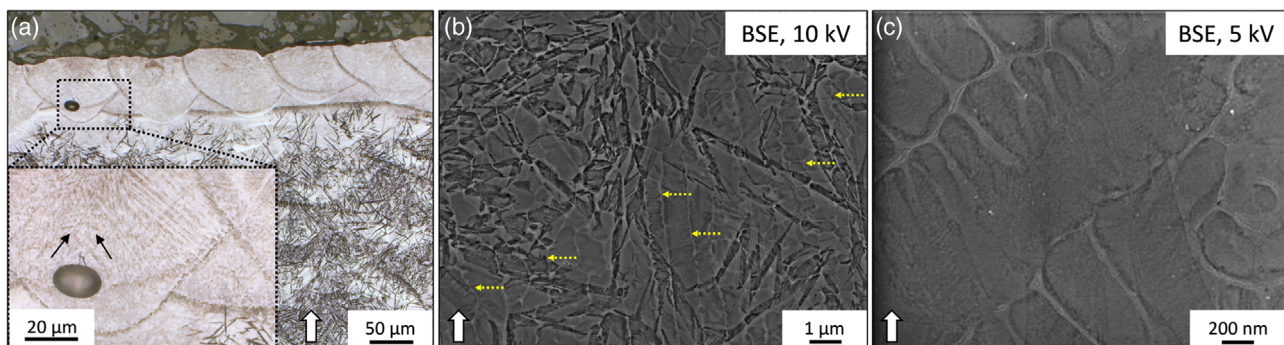


Figure 6. a) LOM overview of the weld bead layer structure. High-resolution SEM images of solidification structure and microstructure in b) a tempered layer and c) the top layer. The black arrows in the inset of (a) indicate the solidification direction, the dashed yellow arrows in (b) indicate a more brightly depicted dendritic network.

the arrows. Figure 6b shows a SEM image of the microstructure of a tempered layer. In addition to the already mentioned needle-like structures, a dendritic network, which is depicted more brightly in the BSE mode of the SEM, is visible. This network is indicated by the dashed yellow arrows in Figure 6b. A high-resolution image of the top layer is shown in Figure 6c. In between the bright dendrite boundaries, extremely fine microstructural constituents can be seen. To clearly identify these constituents, higher magnifications or complementary methods are necessary.

As high-resolution methods, such as transmission electron microscopy (TEM) or APT, would have exceeded the scope of the present work, XRD analysis was carried out to determine the present phases in a representative step specimen sample ($N = 500$). The results of tempered and top layers can be seen in terms of diffractograms in Figure 7a. Rietveld analysis yields an austenite content of 47 wt% for the former and 31 wt% for the latter. No significant carbide peaks can be seen in both diffractograms. Figure 7b shows a magnified view of a distinctive double peak at Bragg angles of $2\theta \approx 81^\circ$ and $2\theta \approx 82^\circ$. These peaks indicate the presence of martensite in the top layers.

To evaluate the influence of tempering processes during LPBF on the hardness of the investigated material, a nanoindentation hardness mapping of the top layers of the sample with 500 layers was carried out, see Figure 8. The black dashed lines indicate melt pool boundaries. It can be clearly extracted that the nanohardness in the last layer is significantly higher than in the underlying in situ tempered layers. No clear correlation between transition zones of adjacent weld beads can be drawn from the hardness mapping. The region beneath the top left melt pool at a x -position of $\approx 45 \mu\text{m}$ and a distance from the surface of $\approx 65 \mu\text{m}$ shows significantly lower hardness of $\approx 9 \text{ GPa}$ compared to the averaged value of the entire mapping of $10.9 \pm 0.8 \text{ GPa}$.

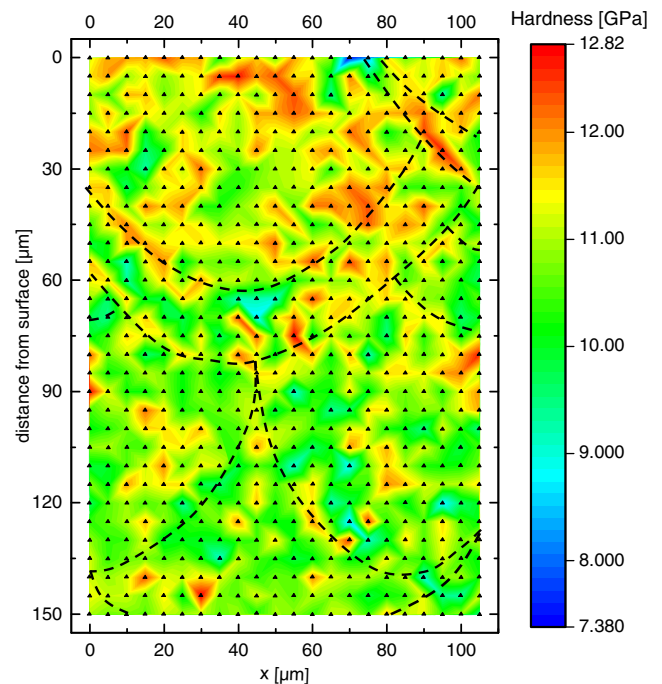


Figure 8. Nanoindentation hardness mapping of the top area of a sample ($N = 500$) manufactured with a VED of 67 J mm^{-3} . The top layers show higher hardness values. No clear correlation between nanohardness and melt pool boundaries, which are indicated by the black dashed lines, can be drawn.

4. Discussion

The aim of the present work was to investigate the evolution of defect structure (pore and crack formation) in dependence of the applied VED during LPBF of a high-alloyed cold-work tool steel.

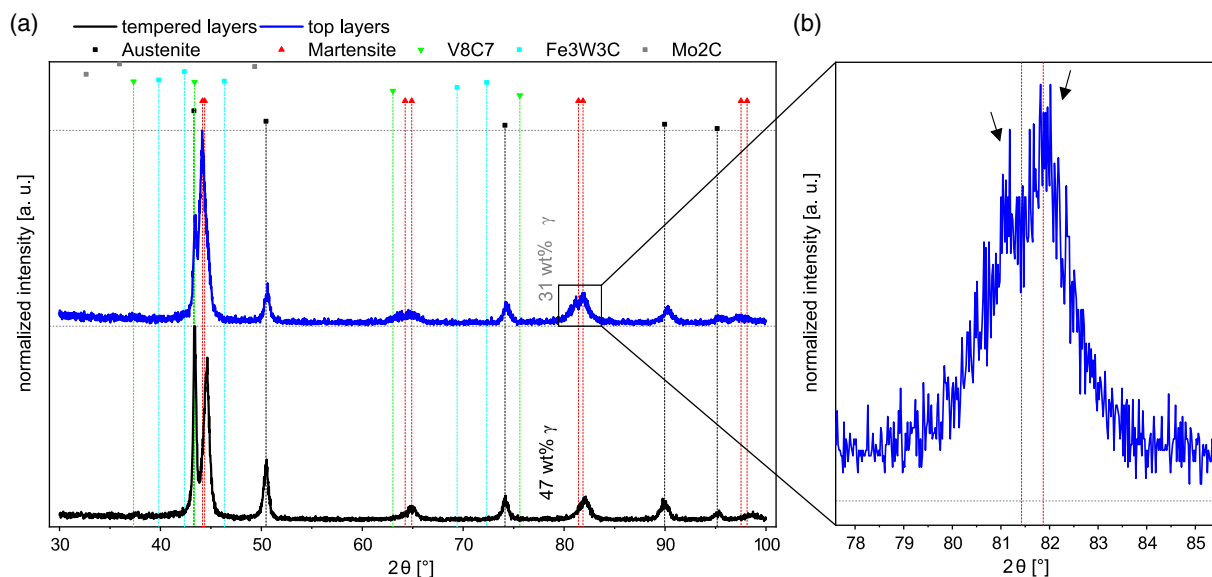


Figure 7. XRD of a) tempered and top layers and b) detailed view of adjacent double peaks (indicated by the black arrows) of the martensite in the top layers of a sample ($N = 500$) manufactured with a VED of 67 J mm^{-3} . The tempered layers show higher austenite content in comparison to the top layers.

In addition to general processability of the used powder, different samples heights were evaluated in terms of their thermal history with regard to crack formation. Most recently published investigations^[14–16] on this research field reported cold cracking respectively cracking caused by high thermal gradients as predominant failure mechanism. As hot cracking is also a well-known phenomenon during conventional welding of high-alloyed austenitic steels, particular attention was devoted to the crack surface characterization. In addition, possible correlations between structural elements and the appearance of defects are discussed in the following subchapters.

4.1. Type of Pores in Dependence of the Applied VED

From the results, it could be concluded that the applied energy input determines which type of pores is present. Two main types, namely irregularly shaped lack-of-fusion and spherical keyhole pores, evolve during LPBF. The former are generated during manufacturing with low energy input due to incomplete melting and therefore powder particles remain within these pores, as shown in Figure 4a representing a sample built with a VED of 40 J mm^{-3} . In contrast, Figure 4b show that a very high energy input of 204 J mm^{-3} results in the formation of spherical shaped pores in the sample. Geenen et al.^[16] also concluded round pores in M3:2 high-speed steel samples which have been manufactured with high energy inputs. The formation of such keyhole pores can be attributed to the inclusion of vaporized metal during solidification of the melt caused by excessively high local laser energy input as no internal pores were found in the cross-section of the powder particles after gas atomization, see Figure 1c.

Apparently, both types of pores appear within the sample which was manufactured with a medium VED of 67 J mm^{-3} , as shown in Figure 4c,d. This may be attributed to local differences in the material composition leading to the release of certain phases or elements with low vaporization points in the spherical pores, accompanied by residual lack-of-fusion defects at this level of VED.

Due to the low oxygen amount within the powder in comparison to the oxygen content of 0.1% in the argon process atmosphere during LPBF, no oxidation in keyhole pores was detected and therefore the dendritic solidification structure within these pores could be clearly seen in Figure 4e. In contrast, the oxidized surface of a lack-of-fusion pore in Figure 4c can be attributed to the aforementioned high oxygen fraction in the process atmosphere. This gas is entrapped in these pores during incomplete melting of the powder due to very low local energy input.

4.2. Predominant Cracking Mechanism

The macroscopic overview in Figure 2 revealed significant differences in terms of crack severity for different sample heights. The exemplary LOM image in Figure 3c revealed that crack origination positions are basically identical for all investigated sample heights. In addition, it was demonstrated that cracks originate at certain positions, such as the transition zone to the building platform, pores, and sample edges. The zig-zag movement of the crack originating from the sample edge in Figure 4d indicated

crack propagation along a defined path. A closer look on another crack in Figure 4e visualized that this path clearly runs along dendrite boundaries. Therefore, crack propagation can be correlated to changes in the solidification direction of primary dendrite packages. In addition, the presence of freely solidified secondary dendrites can be seen, which suggests hot cracking as predominant cracking mechanism within the investigated material.^[23] Furthermore, all cracks propagate upward which could also be extracted from the macroscopic overviews shown in Figure 2 and 3. Confirmation of the presence of hot cracks can be obtained from Figure 5 due to the clear visibility of freely solidified dendrites. Figure 5c,d reassured, that irrespective of the chosen energy input, hot cracking is the predominant cracking mechanism. Furthermore, Figure 5 revealed that an entire crack network is existent within the investigated samples and again proved that crack propagation follows the dendritic solidification structure. From a macroscopic point of view, the clear propagation of the cracks toward the top of the specimen can be attributed to the strongly pronounced thermal gradient, which is accompanied by the formation of residual stresses. This gradient mainly evolves due to the strong heat sink caused by the building platform. Therefore, cracks propagate epitaxially upward and follow the solidification direction. Microscopically considered, the direction of heat flow is strongly dependent on the movement strategy respectively direction of the laser during melting which can be seen in the inset of the LOM image in Figure 6a. A further confirmation that the crack propagation can be correlated to the solidification sequence is given by the fact, that the crack surface at the crack initiation position at the edge of the sample (black arrow in Figure 3c) and the surface at a higher position of the sample (white arrow in Figure 3b) provide the same image of freely solidified dendrites indicating hot cracking.

The main stress sources during LPBF are the pronounced thermal gradient, volume contractions during solidification, and shrinkage during cooling. In addition, the formation of carbon martensite, which results in a volume expansion, in adjacent already cooled areas may also contribute. Nevertheless, all of these stresses were clearly too low to cause cracking of low-melting phases within the investigated material because otherwise hot cracks should be present after and between each weld bead layer. This could not be observed and therefore elevated stresses must be generated locally to form cracks. Apparently, these elevated stresses are formed in certain areas of the samples. The results showed that cracks initiate at the transition zone between the building platform and the AM material, from the edges of the samples and from the edges of both pore types. Clearly, these areas offer an increased notch effect resulting in stress concentrations, which lead to crack formation.

Mercelis and Kruth^[30] investigated the influence of part height on residual stress evolution in a selectively laser molten 316L steel and concluded a strong increase of the measured stresses in the top layers with increasing heights. This can be correlated to the results of the present study. The almost symmetrical crack evolution in Figure 3c can be explained by a possible accumulation of the mentioned stress-formation mechanisms resulting in crack propagation after a certain number of layers at the edges of the samples. As seen experimentally, the crack propagation is more pronounced from the base plate toward the top of the specimens with the increase in the layer number.

It can be deduced that the size and the shape of the produced component are also determining factors on the defect formation mechanism.

Krell et al.^[14] reported a mutual dependence of porosity and crack length in which the latter increases at lower porosity values and vice versa. The crack initiation from notched positions, such as pore edges, observed in the present study could explain this phenomenon as residual stresses are relieved by the occurrence of micro cracks yielding low crack lengths in highly porous samples. Otherwise, crack length would rise due to severe macroscopic cracking originating from the edges of the samples if these stresses were not relieved due to micro cracking at pores.

To clarify the drawn assumptions in terms of stress formation and possible accumulations, complementary experiments, that would exceed the scope of the present work, are necessary. Access to synchrotron facilities would provide high-energy XRD (HEXRD), which is a powerful tool to measure and evaluate such stress profiles respectively accumulations and is planned in future work. In addition to stress measurements, similar to those carried out by Bodner et al.,^[31] HEXRD would also introduce the opportunity to correlate spatially resolved phase analysis and texture measurements in reasonable testing times with sufficient grain statistics to the microstructural evolution of the samples.

In contrast to the already discussed solidification structure, no correlation between defect evolution and microstructure can be drawn. Investigations published in the last years^[14–16] reported cold crack formation caused by hard and therefore brittle carbon martensite in combination with high thermal stresses due to the process-related thermal gradient. This could not be confirmed for the investigated alloy in this study for which hot cracking can be definitely assigned as predominant mechanism. These cracks form during solidification, whereas the microstructure is mainly determined during cooling of the already solidified material. In addition, the complex thermal cycle during LPBF, especially in situ tempering processes caused by the application of subsequently built layers, certainly plays an important role in terms of microstructural evolution.

As far as crack reduction or even crack-free fabrication of the investigated alloy with LPBF is concerned, certain adaptations to the process and to the used powder have to be made. First, the thermal gradient has to be reduced to decrease residual stresses within the material. This can be guaranteed by preheating the platform. Second, a significant reduction in certain elements (mainly sulfur and phosphorus) is necessary to prevent the formation of low-melting phases that cause hot cracking. The latter can be either realized by remelting processes of the atomization feedstock material or by usage of exceptionally pure raw materials during atomization. Finally, constructive adaptations, which lead to a softening of sharp notches and thus to a reduction of stresses, could contribute to a reduction in crack formation.

4.3. Microstructural Evolution

The results showed that the microstructure comprises of three constituents. First, the needle-like phase could be verified to be tempered martensite due to the presence of two adjacent peaks in the diffractograms in Figure 7 and due to the shown LOM and SEM images in Figure 6. Second, the XRD

measurements also proved that, within tempered as well as top layers, significant amounts of retained austenite exist. Therefore, the bright phase in Figure 6a could be clearly assigned to austenite. Third, possible carbide peaks ($\text{Fe}_3\text{W}_3\text{C}$ or V_8C_7) in the shown diffractograms at an 2θ angle of $\approx 43^\circ$ might be overlapped by the distinctive (111)-austenite peak. However, the carbide network was clearly identified in the SEM images in Figure 6b,c. The overlap of these carbide peaks with the distinct (111)-austenite peak in the XRD diffractogram in Figure 7 could be a possible explanation for the high austenite content which could actually represent a combined content comprising of austenite and carbide network. Basically, these three constituents are the same as those present in conventionally manufactured and fully heat-treated cold-work tool steel. However, a clear difference is obvious in the present carbide morphology. The extremely fine carbide network in contrast to homogeneously distributed μm -sized primary carbides that form during conventional manufacturing^[32] can be attributed to the rapid solidification during LPBF. This carbide network mainly comprises of heavy carbide-forming elements, such as W or Mo. This conclusion can be drawn as heavy elements cause enhanced signal and are therefore illustrated more brightly in the SEM images taken in BSE mode^[33] in Figure 6b,c, respectively. Liu et al.^[34] conducted energy-dispersive X-ray spectroscopy measurements in different regions of a selectively laser molten M2 HSS ($\approx \text{HS6-5-2}$ with ≈ 0.9 wt% carbon). Although this steel grade contains higher amounts of carbide-forming elements than the investigated cold-work tool steel, it can be compared in terms of carbon content and therefore carbide formation mechanisms during LPBF. In addition, Liu et al. revealed the presence of a continuous carbide network in the M2 HSS. Further investigations dealing with additively manufactured M2 HSS also concluded the presence of a carbide network.^[35]

In addition to the melt pool structure, which is the characteristic feature for AM materials, Figure 6a clearly showed that the top layers exhibit a different microstructure. In comparison to underlying layers, the top layers lack needle-like martensitic structures. As these layers are not tempered by subsequently built ones, an even more supersaturated condition can be assumed which would manifest itself in a lowering of the martensite start temperature below room temperature. However, the already mentioned adjacent double peaks of the body-centered cubic phase in the XRD diffractogram in Figure 7b prove that the martensitic phase is present. In addition, the phase quantifications show that the austenite content within the top layers is even lower than in the tempered layers. It can therefore be assumed that the microstructural constituents between the dendrite network in Figure 6c are even finer martensitic structures combined with decreased amounts of retained austenite. In addition, the nanohardness mapping in Figure 8 revealed that the hardness of the top layer significantly exceeds that of underlying layers. The local drop in hardness at the bottom of the top weld bead layer may be attributed to an underlying pore, similar to the keyhole pore shown at the bottom of the top layer in the inset of Figure 6a. The general hardness increase in the top layer can be mainly attributed to the lack of tempering as no further layers are manufactured. Unlike the top layer, underlying layers are subjected to such tempering processes, which in turn lead to relaxation of residual stresses and thus to a reduction in hardness.

Furthermore, the higher hardness of the top layer can be eventually assigned to the finer microstructure which is in this case determined by the dendrite network compared with the coarser needle-like martensitic structure in tempered layers. An additional explanation may be given by the aforementioned lower austenite content in the top layer, leading to larger fractions of hard martensite. Krakhmalev et al.^[36] also measured lower values of retained austenite within the top layers of an AISI 420 steel (\approx X44Cr13) compared to inner regions of the LPBF material. They explained the increased austenite content of the latter by an in situ heat treatment caused by the application of subsequently built layers. According to their research work, this in situ tempering treatment enables diffusion processes inducing carbon partitioning, which in turn may trigger austenite reversion.

5. Conclusion

The present work aimed to shed light on the evolution of defect structure in a selectively laser molten cold-work tool steel in dependence of the applied VED. To find possible correlations between defect formation and structural evolution, LOM and SEM investigations were performed in the immediate vicinity of pores and cracks. In addition, crack surfaces were characterized by means of SEM to clearly identify the predominant cracking mechanism. Complementary methods, such as XRD and nanoindentation, were conducted to characterize the microstructure in the as-built condition. The following conclusions can be drawn: 1) Porosity formation is determined by the applied VED. Insufficient energy input yields so-called lack-of-fusion pores. In contrast, excessively high energy input leads to the formation of keyhole pores due to inclusion of vaporized metal by the melt during solidification. To build samples with moderate porosity, a VED in the range of 70 J mm^{-3} should be chosen. Further parameter studies may lead to reduced porosity. 2) Although recently published investigations on LPBF of tool steels assumed cold cracking during LPBF, the present work clearly showed that within the investigated material, irrespective of the chosen VED, hot cracking can be assigned as predominant cracking mechanism due to the presence of freely solidified dendrites on the crack surfaces. Crack evolution can be correlated to the solidification structure as all cracks in the characterized samples propagate toward the top of the specimens. This can be attributed to the strongly pronounced process-related temperature gradient which is accompanied by the formation of thermal stresses. Internal pores, the transition zone between the building platform and the AM material and the edges of the samples act as starting points for the cracks. At these positions, enhanced stresses are generated due to notch effects. Furthermore, the increased occurrence and severity of cracks in higher specimens compared with lower ones can presumably be attributed to a varying thermal history that may lead to possible stress accumulations due to the build-up of many layers. 3) A previously expected connection between crack initiation near hard martensitic structures and process-related thermal stresses could not be determined. 4) The microstructure comprises of tempered martensite, retained austenite, and an extraordinarily fine dendritic carbide network which was formed during rapid solidification. Special

interest was drawn to the characterization of the top layers which differ from underlying layers because they lack subsequent tempering. This causes higher hardness and reduced austenite contents within the top areas of the specimens. 5) In order to reduce or even avoid cracking during LPBF of the investigated cold-work tool steel, the thermal gradient and therefore the evolution of stresses within the single layers should be reduced. During LPBF, this could be achieved by applying a preheating of the building platform. Furthermore, the contents of certain elements (e.g., sulfur or phosphorus), which are decisively involved in hot crack formation, should also be reduced significantly which could be done by means of remelting processes or using particularly pure raw materials in advance to the atomization process. 6) Further investigations concerning stress evolution and possible accumulations, that are possibly caused by varying thermal history induced by different sample heights, are planned to be investigated by means of HEXRD. These experiments are also intended to clarify a possible release of thermal stresses that may lead to the formation of a crack network.

Acknowledgements

The authors gratefully acknowledge funding from the Austrian BMK (846933) in the framework of the program "Production of the future" and the "BMK Professorship for Industry". The Italian Ministry of Education, University and Research is acknowledged for the support provided through the Project "Department of Excellence LIS4.0 – Lightweight and Smart Structures for Industry 4.0". In addition, the authors thank Marco Anilli for his help through the fabrication of samples investigated in this study.

Conflict of Interest

The authors declare no conflict of interest.

Keywords

cold-work tool steels, hot cracking, laser powder bed fusion, microstructures, porosity, selective laser melting, volumetric energy density

Received: July 10, 2020

Revised: October 9, 2020

Published online:

-
- [1] D. Herzog, V. Seyda, E. Wycisk, C. Emmelmann, *Acta Mater.* **2016**, 117, 371.
 [2] B. P. Conner, G. P. Manogharan, A. N. Martof, L. M. Rodomsky, C. M. Rodomsky, D. C. Jordan, J. W. Limperos, *Addit. Manuf.* **2014**, 1, 64.
 [3] a) SLM Solutions GmbH Homepage, www.slm-solutions.com (accessed: February 2020); b) DMG MORI AG Homepage, https://at.dmgmori.com (accessed: August 2020).
 [4] C. Körner, *Int. Mater. Rev.* **2016**, 61, 361.
 [5] H. P. Tang, G. Y. Yang, W. P. Jia, W. W. He, S. L. Lu, M. Qian, *J. Mater. Sci. Eng. A* **2015**, 636, 103.

- [6] a) D. D. Gu, W. Meiners, K. Wissenbach, R. Poprawe, *Int. Mater. Rev.* **2012**, 57, 133; b) P. K. Gokuldoss, S. Kolla, J. Eckert, *Materials* **2017**, 10, 672.
- [7] J. P. Kruth, S. Kumar, J. van Vaerenbergh, *Rapid Prototyp. J.* **2005**, 11, 287.
- [8] J. Sander, J. Hufenbach, L. Giebeler, H. Wendrock, U. Kühn, J. Eckert, *Mater. Des.* **2016**, 89, 335.
- [9] M. Mazur, M. Leary, M. McMillan, J. Elambasseril, M. Brandt, *Rapid Prototyp. J.* **2016**, 22, 504.
- [10] a) R. Casati, J. Lemke, A. Tuissi, M. Vedani, *Metals* **2016**, 6, 218; b) D. Crococolo, M. de Agostinis, S. Fini, G. Olmi, A. Vranic, S. Ciric-Kostic, *Fatigue Fract. Eng. Mater. Struct.* **2016**, 39, 637; c) K. Kempen, E. Yasa, L. Thijs, J.-P. Kruth, J. van Humbeeck, *Phys. Procedia* **2011**, 12, 255; d) Y. Bai, Y. Yang, M. Zhang Di Wang, *J. Mater. Sci. Eng. A* **2017**, 703, 116.
- [11] H. Chen, D. Gu, D. Dai, C. Ma, M. Xia, *J. Mater. Sci. Eng. A* **2017**, 682, 279.
- [12] H. Fayazfar, M. Salarian, A. Rogalsky, D. Sarker, P. Russo, V. Paserin, E. Toyserkani, *Mater. Des.* **2018**, 144, 98.
- [13] R. Mertens, B. Vrancken, N. Holmstock, Y. Kinds, J.-P. Kruth, J. van Humbeeck, *Phys. Procedia* **2016**, 83, 882.
- [14] J. Krell, A. Röttger, K. Geenen, W. Theisen, *J. Mater. Process. Technol.* **2018**, 255, 679.
- [15] J. Boes, A. Röttger, C. Mutke, C. Escher, W. Theisen, *Addit. Manuf.* **2018**, 23, 170.
- [16] K. Geenen, A. Röttger, F. Feld, W. Theisen, *Addit. Manuf.* **2019**, 28, 585.
- [17] J. Saewe, C. Gayer, A. Vogelpoth, J. H. Schleifenbaum, *Berg-Huettenmaenn. Monatsh.* **2019**, 164, 101.
- [18] F. Feuerhahn, A. Schulz, T. Seefeld, F. Vollertsen, *Phys. Procedia* **2013**, 41, 843.
- [19] a) J. Gussone, G. Garces, J. Haubrich, A. Stark, Y.-C. Hagedorn, N. Schell, G. Requena, *Scr. Mater.* **2017**, 130, 110; b) L. Caprio, A. G. Demir, G. Chiari, B. Previtali, *J. Phys. Photonics* **2020**, 2, 24001.
- [20] J. Jin, R. Gao, H. Peng, H. Guo, S. Gong, B. Chen, *Metall. Mater. Trans. A* **2020**, 61, 361.
- [21] E. Folkhard, *Metallurgie der Schweißung Nichtrostender Stähle*, Springer-Verlag, Wien, Austria **1984**.
- [22] a) G. Schulze, in *Die Metallurgie des Schweißens: Eisenwerkstoffe – Nichteisenmetallische Werkstoffe*, Springer, Heidelberg, New York **2010**; b) H. Berns, W. Theisen, in *Eisenwerkstoffe – Stahl und Gusseisen*, Springer, Berlin, Heidelberg **2008**.
- [23] M. Wolf, H. Schobbert, T. Böllinghaus, in *Hot Cracking Phenomena in Welds* (Eds: A. J. Ramirez, J. C. Lippold), Springer, Berlin, Germany **2005**, pp. 245–268.
- [24] M. Cloots, P. J. Uggowitzer, K. Wegener, *Mater. Des.* **2016**, 89, 770.
- [25] A. Matsunawa, J.-D. Kim, N. Seto, M. Mizutani, S. Katayama, *J. Laser Appl.* **1998**, 10, 247.
- [26] A. G. Demir, B. Previtali, *Int. J. Adv. Manuf. Technol.* **2017**, 93, 2697.
- [27] ASTM B212-17, *Standard Test Method for Apparent Density of Free-Flowing Metal Powders Using the Hall Flowmeter Funnel*, ASTM International, West Conshohocken, PA **2017**.
- [28] S. Kumar, in *Comprehensive Materials Processing*, Vol. 10 (Ed: S. Hashmi), Newnes, Oxford **2014**, pp. 93–134.
- [29] WebElements: THE periodic table on the WWW, www.webelements.com/iron/ (accessed: March 2020).
- [30] P. Mercelis, J.-P. Kruth, *Rapid Prototyp. J.* **2006**, 12, 254.
- [31] S. C. Bodner, L. T. G. van de Vorst, J. Zalesak, J. Todt, J. F. Keckes, V. Maier-Kiener, B. Sartory, N. Schell, J. W. Hooijmans, J. J. Saurwalt, J. Keckes, *Addit. Manuf.* **2020**, 32, 101027.
- [32] G. A. Roberts, R. Kennedy, G. Krauss, *Tool Steels*, ASM International, Materials Park, OH **1998**.
- [33] J. I. Goldstein, D. E. Newbury, J. R. Michael, N. W. M. Ritchie, J. H. J. Scott, D. C. Joy, *Scanning Electron Microscopy and X-Ray Microanalysis*, Springer, New York **2017**.
- [34] Z. H. Liu, D. Q. Zhang, C. K. Chua, K. F. Leong, *Mater. Charact.* **2013**, 84, 72.
- [35] a) H. J. Niu, I. T. H. Chang, *J. Mater. Sci.* **2000**, 35, 31; b) H. Asgharzadeh, A. Simchi, *J. Mater. Sci. Eng. A* **2005**, 403, 290; c) C. S. Wright, M. Youseffi, S. P. Akhtar, T. H. C. Childs, C. Hauser, P. Fox, *Mater. Sci. Forum* **2006**, 514516, 516.
- [36] P. Krakhmalev, I. Yadroitsava, G. Fredriksson, I. Yadroitsev, *Mater. Des.* **2015**, 87, 380.